
Nutrient Availability and Immune Cytotoxic Strength Determine Tumor Control Versus Escape: A Spatiotemporal Reaction–Diffusion Analysis

[Maduabuchi Orakwelu](#)*

Posted Date: 21 May 2026

doi: 10.20944/preprints202605.1448.v1

Keywords: tumor microenvironment; immune evasion; tumor–immune–nutrient dynamics; spatiotemporal modeling; reaction–diffusion; necrotic core; immunotherapy; tumor dormancy; mathematical oncology; immune cytotoxicity threshold



Preprints.org is a free multidisciplinary platform providing preprint service that is dedicated to making early versions of research outputs permanently available and citable. Preprints posted at Preprints.org appear in Web of Science, Crossref, Google Scholar, Scilit, Europe PMC, OpenAlex.

Copyright: This open access article is published under a [Creative Commons CC BY 4.0 license](#), which permit the free download, distribution, and reuse, provided that the author and preprint are cited in any reuse.

Disclaimer/Publisher's Note: The statements, opinions, and data contained in all publications are solely those of the individual author(s) and contributor(s) and not of MDPI and/or the editor(s). MDPI and/or the editor(s) disclaim responsibility for any injury to people or property resulting from any ideas, methods, instructions, or products referred to in the content.

Article

Nutrient Availability and Immune Cytotoxic Strength Determine Tumor Control Versus Escape: A Spatiotemporal Reaction–Diffusion Analysis

Maduabuchi Orakwelu 

University of Arkansas Clinton School of Public Service, 1200 President Clinton Ave, Little Rock, AR 72201, United States of America; gorakwelu@clintonschool.uasys.edu

Abstract

Understanding the conditions under which the immune system can suppress or fail to contain a growing tumor remains a central open problem in oncology, with direct implications for the design of immunotherapy protocols. Nutrient availability in the tumor microenvironment is increasingly recognized as a determinant of both tumor aggressiveness and immune cell efficacy, yet the spatial interplay among tumor proliferation, immune infiltration, and nutrient depletion is difficult to disentangle experimentally. This study employs a rigorously analyzed spatiotemporal reaction–diffusion model to identify the parameter regimes — defined by immune cytotoxic strength χ , tumor-driven immune recruitment η , and nutrient consumption rate θ — that determine whether a tumor is controlled, coexists chronically, or escapes immune surveillance entirely. Equilibrium analysis shows that the tumor-free state is unconditionally unstable, while a chronic coexistence state is locally asymptotically stable, establishing a theoretical basis for the observed persistence of tumors under partial immune control. Numerical simulations under two biologically distinct parameter regimes demonstrate spatially resolved outcomes: in the immune-competent regime, cytotoxic infiltration suppresses tumor growth and maintains nutrient availability, whereas in the aggressive regime, rapid nutrient depletion creates a necrotic core in the spatial interior consistent with avascular solid tumor morphology, while the immune response remains spatially peripheral and functionally insufficient. These findings identify critical thresholds in immune killing rate and nutrient supply below which computational models predict inevitable tumor escape, providing quantitative targets for immunotherapy augmentation strategies. High-order implicit time integration (SSHBBDF, order four, A-stable) ensures the biological fidelity of all simulations by resolving the multiscale stiffness inherent in coupled reaction–diffusion cancer models.

Keywords: tumor microenvironment; immune evasion; tumor–immune–nutrient dynamics; spatiotemporal modeling; reaction–diffusion; necrotic core; immunotherapy; tumor dormancy; mathematical oncology; immune cytotoxicity threshold

1. Introduction

The failure of the immune system to eliminate a growing tumor — a phenomenon termed immune escape — is one of the central unsolved problems in cancer biology and a primary obstacle to durable immunotherapy responses [14,22]. In solid tumors, immune control is not determined solely by the intrinsic cytotoxic capacity of effector cells, but is profoundly shaped by the spatial and metabolic architecture of the tumor microenvironment (TME). Nutrient depletion, in particular, drives the formation of hypoxic and necrotic cores that physically exclude immune infiltration and metabolically exhaust cytotoxic T lymphocytes before they can reach the tumor interior [10,34]. Understanding the quantitative conditions — in terms of immune killing rate, recruitment efficiency, and nutrient consumption — under which immune pressure is sufficient to contain tumor growth is therefore of

direct relevance to the design of immunotherapy regimens and the identification of patients likely to respond to immune checkpoint blockade.

Mathematical modeling has emerged as a powerful tool for investigating these threshold phenomena, because the nonlinear coupling between tumor proliferation, immune dynamics, and nutrient transport makes it difficult to isolate causal mechanisms experimentally [5,15]. A model, as defined by Ayeni [4], is an intellectual construct which represents reality and can be manipulated to predict the consequences of future actions. Spatially resolved reaction–diffusion models are particularly informative because they capture the spatial heterogeneity of solid tumors: the necrotic core, the proliferating rim, and the peripheral immune infiltrate, all of which are clinically observable via imaging [19,38]. The spatial tumor–immune modeling framework builds on Mambili-Mamboundou et al. [26], who studied the interaction of tumour infiltrating cytotoxic lymphocytes with solid tumours using coupled reaction–diffusion equations, and demonstrated the existence of a stable tumour dormant state through stability analysis and numerical simulation.

The present study makes three interconnected contributions. First, we develop and rigorously analyze a three-component spatiotemporal model coupling tumor cell density, cytotoxic immune cell density, and a diffusible nutrient field, establishing positivity, uniform boundedness, and global well-posedness via analytic semigroup theory [17,32]. Second, equilibrium and stability analysis identifies two qualitatively distinct long-term states — a chronically coexisting tumor–immune state and a tumor-dominated escape state — and characterizes the parameter thresholds separating them in terms of biologically interpretable dimensionless groups: the immune cytotoxic strength χ , the tumor-driven immune recruitment ratio η/μ , and the nutrient consumption rate θ . Third, numerical simulations under two representative parameter regimes illustrate these contrasting biological outcomes with spatial resolution, including the formation of a necrotic core under nutrient depletion consistent with avascular solid tumor morphology. To integrate these simulations reliably, the multiscale stiffness arising from widely separated reaction and diffusion timescales is handled by a new class of high-order A-stable implicit integrators (SSHBBDF) constructed via off-grid collocation, whose fourth-order convergence is rigorously verified. The capacity to distinguish immune-controlled tumor suppression from sustained tumor escape has direct implications for therapeutic decision-making, where computational predictions of disease trajectories increasingly inform treatment planning and immunotherapy protocol design.

The remainder of this paper is organized as follows. Section 2 presents the dimensional model, nondimensionalization, and governing equations. Section 3 establishes the analytical properties of the system. Section 4 introduces the SSHBBDF framework and derives specific schemes. Section 5 provides the stability analysis. Section 6 describes the numerical implementation. Section 7 presents results and biological interpretation. Section 8 concludes.

2. Mathematical Formulation

2.1. Dimensional Model

We consider a one-dimensional tissue segment of physical length L_a , representing a vascularized region in which tumor cells, immune cells, and a metabolic nutrient evolve and interact. The spatiotemporal dynamics of tumor cell density $T_a(x_a, t_a)$, immune cell density $I_a(x_a, t_a)$, and nutrient concentration $N_a(x_a, t_a)$ are governed by the dimensional reaction–diffusion system

$$\frac{\partial T_a}{\partial t_a} = D_{T,a} \frac{\partial^2 T_a}{\partial x_a^2} + p_a T_a \left(1 - \frac{T_a}{K_a}\right) - \gamma_a T_a I_a + \alpha_a T_a N_a, \quad (1)$$

$$\frac{\partial I_a}{\partial t_a} = D_{I,a} \frac{\partial^2 I_a}{\partial x_a^2} + \eta_a T_a - \mu_a I_a, \quad (2)$$

$$\frac{\partial N_a}{\partial t_a} = D_{N,a} \frac{\partial^2 N_a}{\partial x_a^2} - \delta_a T_a N_a, \quad (3)$$

for $x_a \in (0, L_a)$ and $t_a > 0$. All dimensional variables and parameters are listed in Table 1. Homogeneous Neumann boundary conditions,

$$\frac{\partial T_a}{\partial x_a} = \frac{\partial I_a}{\partial x_a} = \frac{\partial N_a}{\partial x_a} = 0 \quad \text{at } x_a = 0, L_a, \quad t_a > 0, \quad (4)$$

model a biologically isolated tissue segment in which neither cells nor nutrients flux across the boundaries. The system is closed by nonnegative initial profiles $T_a(x_a, 0) = T_{a,0}(x_a)$, $I_a(x_a, 0) = I_{a,0}(x_a)$, $N_a(x_a, 0) = N_{a,0}(x_a)$.

Table 1. Dimensional variables and parameters for the Tumor–Immune–Nutrient model.

Symbol	Description	Units
x_a	Spatial coordinate	mm
t_a	Time	day
T_a	Tumor cell density	cells/mm ³
I_a	Immune cell density	cells/mm ³
N_a	Nutrient concentration	mmol/mm ³
$D_{T,a}$	Tumor diffusion coefficient	mm ² /day
$D_{I,a}$	Immune diffusion coefficient	mm ² /day
$D_{N,a}$	Nutrient diffusion coefficient	mm ² /day
p_a	Tumor proliferation rate	day ⁻¹
K_a	Tumor carrying capacity	cells/mm ³
γ_a	Immune killing rate	mm ³ /(cells·day)
α_a	Nutrient support coefficient	mm ³ /(mmol·day)
η_a	Immune recruitment rate	day ⁻¹
μ_a	Immune natural decay rate	day ⁻¹
δ_a	Nutrient consumption rate	mm ³ /(cells·day)
L_a	Tissue length	mm

2.2. Nondimensionalization

Following the classical nondimensionalization strategy used in tumor reaction-diffusion models [26,38], we introduce the scalings

$$x = \frac{x_a}{L_a}, \quad t = p_a t_a, \quad T = \frac{T_a}{K_a}, \quad I = \frac{I_a}{I_0}, \quad N = \frac{N_a}{N_0}, \quad (5)$$

where I_0 and N_0 are reference immune and nutrient density scales. The resulting dimensionless parameters are

$$D_T = \frac{D_{T,a}}{p_a L_a^2}, \quad D_I = \frac{D_{I,a}}{p_a L_a^2}, \quad D_N = \frac{D_{N,a}}{p_a L_a^2}, \quad (6)$$

$$\chi = \frac{\gamma_a I_0}{p_a}, \quad \alpha = \frac{\alpha_a N_0}{p_a}, \quad \eta = \frac{\eta_a K_a}{p_a I_0}, \quad \mu = \frac{\mu_a}{p_a}, \quad \theta = \frac{\delta_a K_a}{p_a N_0}. \quad (7)$$

The dimensionless parameters and their biological interpretations are summarized in Table 2.

Table 2. Dimensionless parameters obtained from the nondimensionalization of the Tumor–Immune–Nutrient system.

Parameter	Definition	Biological Interpretation
D_T	$D_{T,a}/(p_a L_a^2)$	Tumor diffusivity ratio
D_I	$D_{I,a}/(p_a L_a^2)$	Immune diffusivity ratio
D_N	$D_{N,a}/(p_a L_a^2)$	Nutrient diffusivity ratio
χ	$\gamma_a I_0/p_a$	Immune cytotoxic strength
α	$\alpha_a N_0/p_a$	Nutrient–tumor coupling strength
η	$\eta_a K_a/(p_a I_0)$	Tumor-driven immune recruitment
μ	μ_a/p_a	Immune natural decay
θ	$\delta_a K_a/(p_a N_0)$	Nutrient consumption by tumor

2.3. The Governing System

The nondimensional Tumor–Immune–Nutrient system on $x \in [0, 1]$, $t > 0$ is

$$T_t = D_T T_{xx} + T(1 - T) - \chi TI + \alpha TN, \quad (8)$$

$$I_t = D_I I_{xx} + \eta T - \mu I, \quad (9)$$

$$N_t = D_N N_{xx} - \theta TN, \quad (10)$$

with no-flux boundary conditions $T_x = I_x = N_x = 0$ at $x = 0, 1$ and nonnegative initial data $T(x, 0) = T_0(x)$, $I(x, 0) = I_0(x)$, $N(x, 0) = N_0(x)$.

The biological mechanisms encoded in (8)–(10) are as follows. Tumor proliferation follows a logistic model modulated by immune-mediated killing at rate χ and nutrient-driven enhancement at rate α . Immune dynamics are governed by tumor-stimulated recruitment at rate η and apoptotic decay at rate μ . The nutrient field diffuses rapidly relative to cellular motion, reflecting the physical reality that $D_N \gg D_T$ for small metabolic substrates, and is consumed by tumor metabolic activity at rate θ . This creates a starvation feedback loop in which high tumor density locally depletes nutrients, subsequently limiting further proliferation and creating spatial heterogeneity.

3. Analytical Properties of the System

3.1. Positivity and Invariant Region

A biologically meaningful model must guarantee that all state variables remain nonnegative and uniformly bounded for all finite time. Both properties follow from standard parabolic comparison arguments.

Theorem 1 (Positivity). *Let $T_0, I_0, N_0 \geq 0$ be continuous on $[0, 1]$. Under homogeneous Neumann boundary conditions, the solution satisfies $T(x, t) \geq 0$, $I(x, t) \geq 0$, $N(x, t) \geq 0$ for all $x \in [0, 1]$, $t > 0$.*

Proof. At $T = 0$ the reaction term in (8) vanishes, and diffusion with no-flux boundaries cannot create negativity. At $I = 0$, equation (9) gives $I_t = \eta T \geq 0$. At $N = 0$, equation (10) gives $N_t = D_N N_{xx} \geq 0$ at interior spatial minima. Hence \mathbb{R}_+^3 is positively invariant. \square

Theorem 2 (Uniform Boundedness). *There exist constants $T_{\max}, I_{\max}, N_{\max} > 0$ depending only on initial data and parameters such that $0 \leq T \leq T_{\max}$, $0 \leq I \leq I_{\max}$, $0 \leq N \leq N_{\max}$ for all $x \in [0, 1]$, $t > 0$.*

Proof. Since $N_t - D_N N_{xx} = -\theta TN \leq 0$, the maximum principle gives $N \leq N_{\max} := \max_x N_0(x)$. Dropping the nonpositive term $-\chi TI$ in (8) and using $N \leq N_{\max}$ yields a logistic upper bound $T \leq T_{\max} := 1 + \alpha N_{\max}$. Finally, with $T \leq T_{\max}$, equation (9) gives $I \leq I_{\max} := \eta T_{\max} / \mu$. The compact rectangular region $\mathcal{E} = [0, T_{\max}] \times [0, I_{\max}] \times [0, N_{\max}]$ is therefore positively invariant. \square

3.2. Well-Posedness of the Reaction–Diffusion System

For completeness, we summarize the analytical properties ensuring that the tumor–immune–nutrient system is mathematically well-defined. Full proofs follow standard results in analytic semigroup theory and are omitted for brevity.

Linear Operator.

Let $U = (T, I, N)^\top$, $X = (L^2(0, 1))^3$, and define the diffusion operator

$$A = \text{diag}(D_T \Delta, D_I \Delta, D_N \Delta),$$

with homogeneous Neumann boundary conditions. Each scalar Laplacian with Neumann boundary conditions is self-adjoint, dissipative, and has compact resolvent. Hence A generates an analytic, contractive C_0 -semigroup on X [17,32].

Nonlinear Reaction Term.

The nonlinear mapping

$$F(U) = \begin{pmatrix} T(1 - T) - \chi TI + \alpha TN \\ \eta T - \mu I \\ -\theta TN \end{pmatrix}$$

is locally Lipschitz on X . On the positively invariant region established in Section 3.1, F is globally Lipschitz since each component is polynomial of degree at most two and all partial derivatives are uniformly bounded on \mathcal{E} .

Global Well-Posedness.

The semilinear evolution equation

$$U_t = AU + F(U), \quad U(0) = U_0 \geq 0,$$

follows the abstract framework developed in Egwurube [16] and extended in Orakwelu et al. [29], where existence, asymptotic stability, and contraction of solutions of evolution equations of the form $du/dt = Au + f(u, t)$ on Banach spaces were established using strongly continuous semigroups and resolvent estimates. Global well-posedness follows from Pazy [32] and Engel and Nagel [17]. The tumor-immune-nutrient PDE system is globally well-posed, positive, and uniformly bounded. These properties guarantee that the model is mathematically consistent and suitable for high-order implicit time integration methods such as the SSHBDF schemes developed in this work.

3.3. Equilibrium Analysis

Setting all time derivatives to zero and neglecting diffusion yields two biologically distinct steady states from the factorization $-\theta T^* N^* = 0$.

The *tumor-free equilibrium* $E_0 = (0, 0, N_0)$ arises when $T^* = 0$, giving $I^* = 0$ and leaving nutrients at homeostatic level N_0 . This represents healthy tissue in which the tumor has been eliminated or failed to establish.

The *coexistence equilibrium* E_1 arises when $T^* \neq 0$, forcing $N^* = 0$ due to complete metabolic exhaustion, and yields

$$T^* = \frac{\mu}{\mu + \chi\eta}, \quad I^* = \frac{\eta}{\mu} T^*, \quad N^* = 0, \quad (11)$$

representing a chronic disease state in which the tumor persists at a size limited by immune pressure despite complete nutrient depletion.

3.4. Local Stability

The Jacobian of the reaction system at (T^*, I^*, N^*) is

$$J = \begin{pmatrix} 1 - 2T^* - \chi I^* + \alpha N^* & -\chi T^* & \alpha T^* \\ \eta & -\mu & 0 \\ -\theta N^* & 0 & -\theta T^* \end{pmatrix}. \quad (12)$$

Theorem 3 (Instability of E_0). *The tumor-free equilibrium $E_0 = (0, 0, N_0)$ is unstable for any $N_0 > 0$.*

Proof. At E_0 the Jacobian is upper triangular with diagonal entries $\lambda_1 = 1 + \alpha N_0 > 0$, $\lambda_2 = -\mu < 0$, $\lambda_3 = 0$. The positive eigenvalue λ_1 implies that any small tumor inoculation will grow initially rather than be cleared. \square

Theorem 4 (Stability of E_1). *The coexistence equilibrium E_1 is locally asymptotically stable.*

Proof. At E_1 with $N^* = 0$, the eigenvalue $\lambda_3 = -\theta T^* < 0$ decouples the nutrient direction. Using the equilibrium relation $1 - T^* - \chi I^* = 0$, the remaining 2×2 tumor-immune block has trace $-T^* - \mu < 0$ and determinant $\mu T^* + \chi \eta T^* > 0$. By the Routh–Hurwitz criterion, all eigenvalues of $J(E_1)$ have negative real parts, confirming local asymptotic stability. \square

4. The SSHBDF Framework

Block methods for differential equations were introduced by Milne [27] and developed by many researchers [11,18,37,40]. To overcome the Dahlquist stability barrier, hybrid block methods incorporating at least one non-integer function evaluation were proposed by Butcher [7], Gear [20], and Gragg and Stetter [21]. The Backward Differentiation Formula, the most widely used class of multistep methods for stiff ODEs, was introduced by Curtiss and Hirschfelder [12]. The multistep collocation approach underlying the SSHBDF derivation follows the continuous interpolant framework established by Adee et al. [1] and Onumanyi et al. [31], who developed hybrid block formulas of order four using non-integer off-grid points to improve starting accuracy, demonstrating that the placement of intra-step evaluation points has a decisive influence on both order and global error. Within the past decade, researchers have clearly demonstrated the dependence of the accuracy of block hybrid methods on the number and placement of grid points in the derivation process [2,28,30,33,35].

We present a class of self-starting SSHBDF of the form

$$\sum_{j=0}^k \alpha_j y_{n+j} + \sum_{\rho=1}^m \alpha_{v_\rho} y_{n+v_\rho} = h \beta_k f_{n+k}, \quad (13)$$

where $k \in \mathbb{Z}^+$, $|\alpha_k| = 1$, and $v_\rho \in (0, k)$ are $m = 2n + 1$, $n = 1, 2, 3, \dots$, equally spaced non-integer off-grid points defined by

$$x_{n+v_\rho} = x_n + \frac{\rho}{m+1} h, \quad \rho = 1, 2, \dots, m. \quad (14)$$

Definition 1. A Single Step Hybrid Block BDF is the coupled system

$$\begin{cases} \sum_{j=0}^k \alpha_j y_{n+j} + \sum_{\rho=1}^m \alpha_{v_\rho} y_{n+v_\rho} = h \beta_k f_{n+k}, \\ \sum_{j=0}^{k-1} \tilde{\alpha}_j y_{n+j} + \sum_{\rho=1}^m \tilde{\alpha}_{v_\rho} y_{n+v_\rho} = h \tilde{\beta}_k f_{n+k} + h \tilde{\beta}_{v_\rho} f_{n+v_\rho}, \quad \hat{\rho} = 1, \dots, m, \end{cases} \quad (15)$$

where all coefficients are determined by the collocation conditions of Section 4.2.

Conjecture 5 (Generalized Intra-Step Optimization Principle). Let $k \geq 1$ and $m = 2n + 1$, $n \in \mathbb{N}$. Define $\mathcal{V}_m = \{v : 0 < v_1 < \dots < v_m < k\}$. Then there exists a nonempty subset $\mathcal{V}_m^* \subseteq \mathcal{V}_m$ such that each $v \in \mathcal{V}_m^*$ yields a hybrid scheme whose leading local truncation error is strictly smaller than that of any other configuration in \mathcal{V}_m , while its stability region satisfies $S_m(v) \supseteq S_m^{\text{BDF}}$.

4.1. Derivation of the Continuous Approximation

We seek a polynomial $Y(t) = \sum_{j=0}^{p+q-1} b_j x^j$, where $p = m + 1$ interpolation points and $q = k$ collocation points determine the degree $p + q - 1$. Coefficients b_j are obtained by imposing interpolation conditions at the $m + 1$ grid and off-grid values,

$$\sum_{j=0}^{m+1} b_j x_{n+v_\rho}^j = y_{n+v_\rho}, \quad \rho = 0, 1, \dots, m, \quad (16)$$

and a collocation condition at x_{n+k} ,

$$\sum_{j=0}^{m+1} j b_j x_{n+k}^{j-1} = f_{n+k}. \quad (17)$$

This system $AB = C$ is solved by matrix inversion. Evaluating $Y(x)$ at x_{n+k} yields the main formula (13), and evaluating $Y'(x)$ at the off-grid points yields the supplementary formulas.

4.2. Specific Schemes

SSHBBDF with $m = 3$.

Setting $k = 1$, $m = 3$, and off-grid points $\{1/4, 1/2, 3/4\}$, the derivation yields the main formula

$$-y_{n+1} - \frac{36}{25}y_{n+\frac{1}{2}} + \frac{16}{25}y_{n+\frac{1}{4}} + \frac{48}{25}y_{n+\frac{3}{4}} - \frac{3}{25}y_n = -\frac{3}{25}hf_{n+1}, \quad (18)$$

together with supplementary formulas at each off-grid point:

$$\frac{26}{25}y_n - \frac{138}{25}y_{n+\frac{1}{2}} + \frac{78}{25}y_{n+\frac{1}{4}} + \frac{34}{25}y_{n+\frac{3}{4}} = \frac{1}{25}hf_{n+1} - hf_{n+\frac{1}{4}}, \quad (19)$$

$$-\frac{12}{25}y_{n+\frac{1}{2}} + \frac{72}{25}y_{n+\frac{1}{4}} - \frac{152}{75}y_{n+\frac{3}{4}} - \frac{28}{75}y_n = -\frac{1}{25}hf_{n+1} - hf_{n+\frac{1}{2}}, \quad (20)$$

$$\frac{34}{75}y_n + \frac{186}{25}y_{n+\frac{1}{2}} - \frac{66}{25}y_{n+\frac{1}{4}} - \frac{394}{75}y_{n+\frac{3}{4}} = \frac{3}{25}hf_{n+1} - hf_{n+\frac{3}{4}}. \quad (21)$$

SSHBBDF with $m = 5$.

Setting $k = 1$, $m = 5$, and off-grid points $\{1/6, 1/3, 1/2, 2/3, 5/6\}$, the analogous collocation derivation yields a 6×6 linear system whose solution gives the coefficient matrices $A_5^{(1)}$, $A_5^{(0)}$, and $B_5^{(1)}$ recorded in Section 5.

5. Analysis of the SSHBBDF Class

5.1. Block Representation

The SSHBBDF update for each block is written as

$$A^{(1)}Y_\omega = A^{(0)}Y_{\omega-1} + hB^{(1)}F_\omega + hB^{(0)}F_{\omega-1}, \quad \omega = 1, 2, \dots, \quad (22)$$

where Y_ω and F_ω are block vectors of solution and function values, and $A^{(1)}$, $A^{(0)}$, $B^{(1)}$, $B^{(0)}$ are $(m+1) \times (m+1)$ matrices. For $m = 3$ these are

$$A^{(1)} = \begin{pmatrix} -\frac{16}{25} & \frac{36}{25} & -\frac{48}{25} & 1 \\ -\frac{78}{25} & \frac{138}{25} & -\frac{34}{25} & 0 \\ -\frac{72}{25} & \frac{12}{25} & \frac{152}{75} & 0 \\ \frac{66}{25} & -\frac{186}{25} & \frac{394}{75} & 0 \end{pmatrix}, \quad A^{(0)} = \begin{pmatrix} 0 & 0 & 0 & \frac{3}{25} \\ 0 & 0 & 0 & -\frac{26}{25} \\ 0 & 0 & 0 & \frac{28}{75} \\ 0 & 0 & 0 & -\frac{34}{75} \end{pmatrix}, \quad (23)$$

$$B^{(1)} = \begin{pmatrix} 0 & 0 & 0 & \frac{3}{25} \\ 1 & 0 & 0 & -\frac{1}{25} \\ 0 & 1 & 0 & \frac{1}{25} \\ 0 & 0 & 1 & -\frac{3}{25} \end{pmatrix}. \quad (24)$$

For $m = 5$, the 6×6 matrices $A_5^{(1)}$, $A_5^{(0)}$, and $B_5^{(1)}$ follow directly from the collocation derivation; their entries are given explicitly in the supplementary material.

5.2. Local Truncation Error

The local truncation error operator associated with the SSHBBDF is

$$L[y(x), h] = \sum_{j=0}^k \alpha_j y(x + jh) + \sum_{\rho=1}^m \alpha_{v_\rho} y(x + v_\rho h) - h \beta_k y'(x + kh) - h \sum_{\hat{\rho}=1}^m \beta_{v_{\hat{\rho}}} y'(x + v_{\hat{\rho}} h). \quad (25)$$

Expanding in Taylor series about x gives $L[y, h] = \sum_{q=0}^{\infty} c_q h^q y^{(q)}(x)$. The method has order p if $c_0 = \dots = c_p = 0$ and $c_{p+1} \neq 0$ [24]. Our calculations demonstrate that the SSHBBDF class achieves high order with reassuringly small error constants. For the SSHBBDF with $m = 3$ and $m = 5$ off-grid points, symbolic computation yields the following principal local truncation error terms for each formula in the block:

$$m(3) = \begin{cases} \frac{3h^5 y^{(5)}(x)}{32000} + O(h^6) \\ -\frac{29h^5 y^{(5)}(x)}{128000} + O(h^6) \\ \frac{31h^5 y^{(5)}(x)}{192000} + O(h^6) \\ -\frac{37h^5 y^{(5)}(x)}{128000} + O(h^6), \end{cases}$$

$$m(5) = \begin{cases} \frac{5h^7 y^{(7)}(x)}{24004512} + O(h^8) \\ -\frac{53h^7 y^{(7)}(x)}{96018048} + O(h^8) \\ \frac{h^7 y^{(7)}(x)}{4445280} + O(h^8) \\ -\frac{167h^7 y^{(7)}(x)}{960180480} + O(h^8) \\ \frac{59h^7 y^{(7)}(x)}{240045120} + O(h^8) \\ -\frac{23h^7 y^{(7)}(x)}{32006016} + O(h^8), \end{cases}$$

$$m(3) : \mathcal{O}(h^5), \quad m(5) : \mathcal{O}(h^7). \quad (26)$$

Since the leading term of the local truncation error is $c_{p+1} h^{p+1} y^{(p+1)}$ for a method of order p [24], the relations in (26) confirm that the SSHBBDF with $m = 3$ is of 4 and the SSHBBDF with $m = 5$ is of 6.

5.3. Zero Stability

As $h \rightarrow 0$, the block system (22) reduces to $A^{(1)} Y_{\omega} = A^{(0)} Y_{\omega-1}$. The first characteristic polynomial of the class is

$$\chi(R) = \det[RA^{(1)} - A^{(0)}] = \xi R^m (1 + R), \quad \xi \in \mathbb{Q}. \quad (27)$$

All roots satisfy $|R_j| \leq 1$ and those with $|R_j| = 1$ have multiplicity one, so the SSHBBDF class is zero stable [30].

5.4. Linear Stability

Applying the SSHBBDF to the test equation $y' = \lambda y$, $\lambda < 0$, yields $Y_{\omega} = D(z) Y_{\omega-1}$ where $D(z) = (A^{(1)} - zB^{(1)})^{-1} A^{(0)}$ and $z = \lambda h$. The stability function $R(z)$ is the dominant eigenvalue of $D(z)$.

For $m = 3$ the stability function is

$$R(z) = -\frac{3z^3 + 44z^2 + 288z + 768}{3z^4 - 25z^3 + 140z^2 - 480z + 768}. \quad (28)$$

For $m = 5$ the stability function is

$$R(z) = -\frac{2(5z^5 + 137z^4 + 2025z^3 + 18360z^2 + 97200z + 233280)}{10z^6 - 147z^5 + 1624z^4 - 13230z^3 + 75600z^2 - 272160z + 466560}. \quad (29)$$

The stability regions defined by $|R(z)| \leq 1$ are plotted in Figures 1 and 1. The SSHBBDF with $m = 3$ is A-stable, as the stability region contains the entire left half-plane. The scheme with $m = 5$ is L_0 -stable [9], satisfying $\max_{z \leq 0} |R(z)| \leq 1$ and $\lim_{z \rightarrow -\infty} R(z) = 0$.

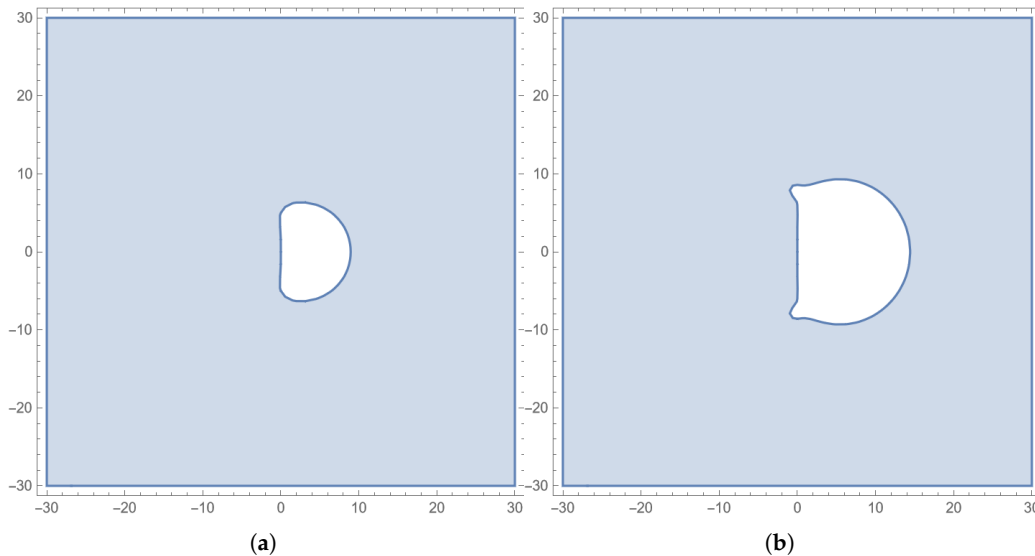


Figure 1. This is a wide figure. Schemes follow the same formatting. If there are multiple panels, they should be listed as: (a) Description of what is contained in the first panel. (b) Description of what is contained in the second panel. (c) Description of what is contained in the third panel. (d) Description of what is contained in the fourth panel. Figures should be placed in the main text near to the first time they are cited. A caption on a single line should be centered.

6. Numerical Implementation

6.1. Method of Lines Spatial Discretization

We discretize the spatial domain $[0, 1]$ using a uniform grid of $M + 1$ nodes $x_i = i\Delta x$, $\Delta x = 1/M$, $i = 0, \dots, M$. The Laplacian is approximated by standard second-order central differences,

$$\frac{\partial^2 U}{\partial x^2} \Big|_{x_i} \approx \frac{U_{i+1}(t) - 2U_i(t) + U_{i-1}(t)}{(\Delta x)^2}, \quad (30)$$

with ghost points enforcing the Neumann conditions: $U_{-1} = U_1$ and $U_{M+1} = U_{M-1}$, giving modified boundary stencils

$$\Delta U \Big|_{x_0} \approx \frac{2U_1 - 2U_0}{(\Delta x)^2}, \quad \Delta U \Big|_{x_M} \approx \frac{2U_{M-1} - 2U_M}{(\Delta x)^2}. \quad (31)$$

Substituting into (8)–(10) yields the semi-discrete system of $3(M + 1)$ coupled ODEs, written compactly as

$$\frac{dY}{dt} = \mathbf{A}Y + F(Y), \quad Y(0) = Y_0, \quad (32)$$

where $Y(t) = [T_0, \dots, T_M, I_0, \dots, I_M, N_0, \dots, N_M]^T \in \mathbb{R}^{3(M+1)}$, \mathbf{A} is the sparse block-diagonal diffusion matrix, and $F(Y)$ contains the nonlinear reaction terms.

6.2. Time Integration

The SSHBBDF schemes are applied to integrate (32). Modified Newton iteration is employed at each time step to handle the nonlinear reaction terms, with the diffusion component treated by Gaussian elimination with partial pivoting. The block structure of the SSHBBDF allows simultaneous evaluation at all off-grid points within each step, enabling natural parallelization and reducing the number of function evaluations relative to sequential approaches.

7. Numerical Results

7.1. Parameter Values

Tables 3 and 4 present two parameter sets representing biologically distinct scenarios. Tumor proliferation rates and immune decay rates follow de Pillis et al. [13], who validated a tumor-immune model against mouse and human chromium release assay data. Diffusion coefficients for tumor cells are consistent with melanoma cell migration measurements reported by Stepien et al. [39], and the nutrient diffusion coefficient is set substantially higher than cellular diffusivities to reflect the rapid equilibration of small metabolic substrates relative to cell-scale motion [19].

Table 3. Parameter set 1: moderate stiffness regime with balanced tumor-immune competition. Values adapted from de Pillis et al. [13].

Parameter	Description	Value	Units
D_T	Tumor diffusion coefficient	1.0×10^{-3}	mm^2/day
D_I	Immune diffusion coefficient	0.005×10^{-3}	mm^2/day
D_N	Nutrient diffusion coefficient	1.0×10^{-2}	mm^2/day
ρ	Tumor proliferation rate	1.0	day^{-1}
K	Tumor carrying capacity	1.0	cells/mm^3
γ	Immune killing rate	1.0	$\text{mm}^3/(\text{cells}\cdot\text{day})$
δ	Nutrient consumption rate	1.0	$\text{mmol}/(\text{cells}\cdot\text{day})$
α	Nutrient support coefficient	1.0	$\text{mm}^3/(\text{cells}\cdot\text{day})$
η	Immune recruitment rate	1.0	day^{-1}
μ	Immune decay rate	0.5	day^{-1}

Table 4. Parameter set 2: high stiffness regime representing aggressive tumor dynamics consistent with immunosuppressive tumors. Values adapted from de Pillis et al. [13] and Stepien et al. [39].

Parameter	Description	Value	Units
D_T	Tumor diffusion coefficient	0.01	mm^2/day
D_I	Immune diffusion coefficient	0.1	mm^2/day
D_N	Nutrient diffusion coefficient	0.5	mm^2/day
ρ	Tumor proliferation rate	0.8	day^{-1}
K	Tumor carrying capacity	1,000,000	cells/mm^3
γ	Immune killing rate	1.5×10^{-7}	$\text{mm}^3/(\text{cells}\cdot\text{day})$
δ	Nutrient consumption rate	2.0×10^{-7}	$\text{mmol}/(\text{cells}\cdot\text{day})$
α	Nutrient support coefficient	1.5×10^{-7}	$\text{mm}^3/(\text{cells}\cdot\text{day})$
η	Immune recruitment rate	0.2	day^{-1}
μ	Immune decay rate	0.1	day^{-1}

7.2. Convergence Verification

Since this is the first numerical study of this exact three-component Tumor-Immune-Nutrient system, no reference solution from the prior literature is available. Temporal convergence is therefore assessed through a four-level Richardson step-doubling procedure using successively halved time-step sizes $\Delta t \in \{0.01, 0.005, 0.0025, 0.00125\}$. All solutions are evaluated at the shared output point $T_{\text{final}} = 1$, the unique grid point common to all four meshes, which eliminates interpolation error entirely. The off-grid stage values at $t + h/4$, $t + h/2$, $t + 3h/4$ are internal block quantities and are excluded from the comparison.

The Experimental Order of Convergence (EOC) is estimated via

$$\text{EOC} = \log_2 \left(\frac{\|Y^{\Delta t} - Y^{\Delta t/2}\|}{\|Y^{\Delta t/2} - Y^{\Delta t/4}\|} \right), \quad (33)$$

where the norm $\|\cdot\|$ is evaluated over all $N = 60$ spatial nodes at T_{final} . Three norms are computed in parallel to confirm robustness of the estimate:

$$\|\mathbf{d}\|_{\infty} = \max_{1 \leq j \leq 60} |d_j|, \quad \|\mathbf{d}\|_2 = \left(\sum_{j=1}^{60} |d_j|^2 \right)^{1/2}, \quad \|\mathbf{d}\|_1 = \sum_{j=1}^{60} |d_j|, \quad (34)$$

where $d_j = |Y_j^{\Delta t} - Y_j^{\Delta t/2}|$ is the pointwise difference at node j . The four step sizes yield three successive difference vectors

$$\mathbf{d}_{12} : \Delta t = 0.01 \rightarrow 0.005, \quad \mathbf{d}_{23} : \Delta t = 0.005 \rightarrow 0.0025, \quad \mathbf{d}_{34} : \Delta t = 0.0025 \rightarrow 0.00125,$$

and two independent EOC estimates,

$$\text{EOC}_1 = \log_2 \frac{\|\mathbf{d}_{12}\|}{\|\mathbf{d}_{23}\|}, \quad \text{EOC}_2 = \log_2 \frac{\|\mathbf{d}_{23}\|}{\|\mathbf{d}_{34}\|}.$$

Table 5 records the global EOC values under all three norms. All six estimates lie in the narrow band $[3.98, 4.00]$, in excellent agreement with the theoretical order $p = 4$ of the SSHBDF scheme with $m = 3$, as established analytically in Section 7.2. The values of EOC_2 are marginally closer to 4.0 than those of EOC_1 , consistent with asymptotic convergence: as Δt decreases, higher-order error terms become negligible and the EOC converges monotonically toward the true order $p = 4$. The minor deviation from 4.0 at coarser refinement levels is a preasymptotic effect fully expected for finite step sizes.

Table 5. Global EOC at $T_{\text{final}} = 1$ via four-level Richardson step-doubling (33) under three norms. Theoretical order: $p = 4$ (SSHBDF, $m = 3$).

Norm	EOC_1 ($\Delta t: 0.01 \rightarrow 0.0025$)	EOC_2 ($\Delta t: 0.005 \rightarrow 0.00125$)	Theoretical
Max-norm $\ \cdot\ _{\infty}$	3.9889	3.9945	4
L^2 -norm $\ \cdot\ _2$	3.9874	3.9937	4
L^1 -norm $\ \cdot\ _1$	3.9845	3.9922	4

Figure 2 shows the three pointwise difference vectors $|\mathbf{d}_{12}|$, $|\mathbf{d}_{23}|$, and $|\mathbf{d}_{34}|$ across all 60 spatial nodes. The successive geometric reduction in magnitude as Δt is halved is visually pronounced: each curve lies approximately $2^4 = 16$ times below the previous one, which is the hallmark signature of a 4th-order scheme and provides direct graphical confirmation of the values in Table 5. The y -axis upper bound of 1.62×10^{-12} at the finest refinement level reflects the very high absolute accuracy achieved.

Figure 3 overlays the pointwise EOC_1 and EOC_2 at each spatial node $j = 1, \dots, 60$. Both curves cluster tightly around the theoretical value $p = 4$ across the entire spatial domain, demonstrating that convergence is spatially uniform and not merely an average effect. The EOC_2 curve sits marginally closer to the reference line, confirming the expected asymptotic behaviour. Isolated spikes near $j = 18$ and $j = 55$ – 56 occur where the solution value is very close to zero, making the ratio of successive differences sensitive to floating-point rounding; they carry no physical significance and do not indicate a local loss of accuracy.

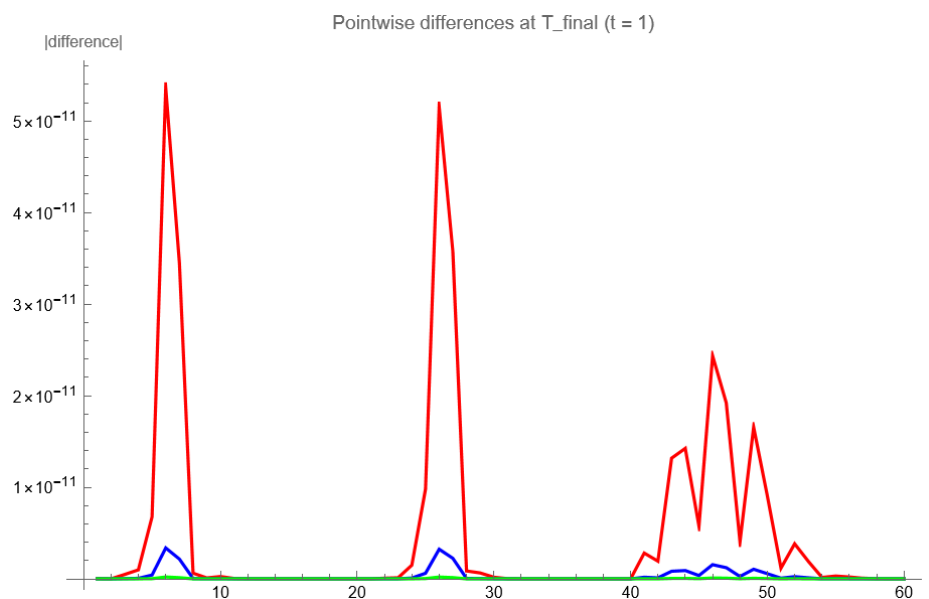


Figure 2. Pointwise differences $|d_{12}|$ ($\Delta t : 0.01 \rightarrow 0.005$, red), $|d_{23}|$ ($\Delta t : 0.005 \rightarrow 0.0025$, blue), and $|d_{34}|$ ($\Delta t : 0.0025 \rightarrow 0.00125$, green) at $T_{\text{final}} = 1$ across all 60 spatial nodes. Each successive curve is approximately $2^4 = 16$ times smaller than the previous, confirming 4th-order convergence in Δt .

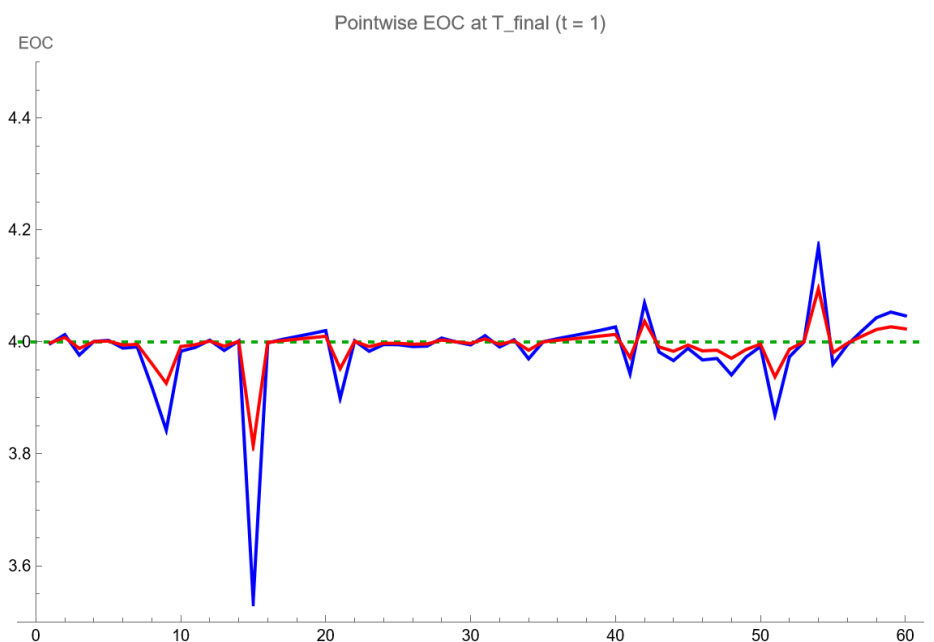


Figure 3. Pointwise EOC_1 ($\Delta t : 0.01 \rightarrow 0.005 \rightarrow 0.0025$, blue) and EOC_2 ($\Delta t : 0.005 \rightarrow 0.0025 \rightarrow 0.00125$, red) at $T_{\text{final}} = 1$ across all 60 spatial nodes. Both curves cluster uniformly around the theoretical order $p = 4$ (dashed reference line), confirming spatially uniform 4th-order convergence of the SSHBDF scheme with $m = 3$. The EOC_2 curve lies marginally closer to $p = 4$, consistent with asymptotic convergence.

7.3. Spatiotemporal Dynamics

Figures 4 and 5 present three-dimensional spatiotemporal plots of tumor density, nutrient concentration, and immune density under the two parameter regimes.

Under parameter set 1, tumor density decreases in regions of high immune activity and nutrient availability, indicating effective immunological suppression. The immune population concentrates near the tumor boundary, and nutrient levels remain sufficient to sustain ongoing immune function.

The system evolves toward the stable coexistence equilibrium E_1 , in which tumor size is limited by immune pressure rather than by metabolic exhaustion.

Under parameter set 2, sustained tumor expansion overwhelms the immune response. Rapid nutrient depletion creates a nutrient-starved core in the spatial interior, consistent with the necrotic cores observed in solid avascular tumors [19,38]. The immune density remains low and spatially peripheral, unable to penetrate the metabolically depleted region. This regime demonstrates therapeutic failure and corresponds dynamically to growth toward a tumor-dominated state far from E_1 .

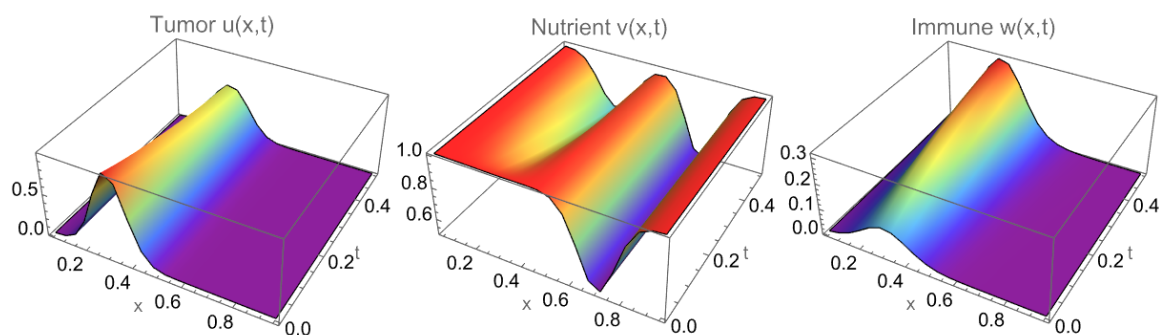


Figure 4. Spatiotemporal dynamics under parameter set 1 (Table 3). From left to right: tumor density $T(x,t)$, nutrient concentration $N(x,t)$, and immune density $I(x,t)$. Effective immune control suppresses tumor growth and maintains nutrient availability.

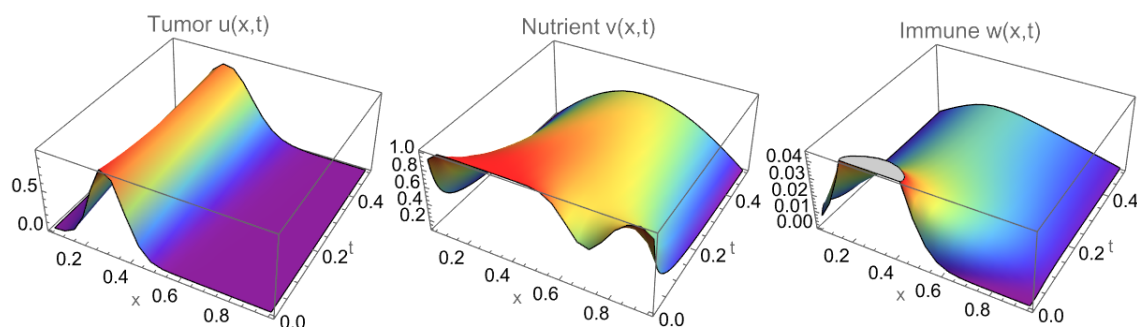


Figure 5. Spatiotemporal dynamics under parameter set 2 (Table 4). Aggressive tumor growth depletes nutrients in the spatial interior, creating a necrotic core, while the immune response remains insufficient to control expansion.

8. Conclusion

This study investigated the conditions under which cytotoxic immune responses can suppress solid tumor growth versus being overwhelmed by aggressive expansion and metabolic competition. The central biological finding is that the outcome — immune-mediated control or tumor escape — is determined by a combination of three dimensionless parameters: the immune cytotoxic strength χ , the tumor-driven immune recruitment ratio η/μ , and the nutrient consumption rate θ . When χ and η/μ are sufficiently large relative to θ , the system evolves toward the chronic coexistence equilibrium E_1 , in which immune pressure limits tumor size despite complete nutrient depletion at steady state. When these conditions are not met, rapid nutrient exhaustion creates a metabolically hostile interior that excludes immune infiltration, generating a spatially peripheral immune response and a necrotic core consistent with avascular solid tumor morphology observed clinically.

These results have direct implications for immunotherapy design. The instability of the tumor-free equilibrium E_0 — which holds for any positive nutrient level — establishes mathematically that passive immune surveillance alone is insufficient to eliminate an established tumor, consistent with clinical experience. The stability of E_1 suggests that partial immune control, rather than eradication, may be the achievable target in many solid tumor contexts, and that interventions which boost χ (e.g.,

checkpoint inhibitors) or η (e.g., adoptive cell transfer) may shift a patient from the escape regime into the controllable coexistence regime. The spatial simulations further suggest that nutrient competition — and therefore anti-angiogenic or metabolic co-therapies — may critically affect whether immune cells can physically access the tumor interior.

The mathematical framework supporting these conclusions is rigorous: positivity, uniform boundedness, global well-posedness, and local asymptotic stability of E_1 are all established analytically. Numerical simulations are performed using a fourth-order A-stable SSHBDF implicit integrator, whose convergence is verified to fourth order across all spatial nodes and three norms (EOC $\in [3.98, 4.00]$), ensuring that all reported dynamics reflect the true behavior of the biological model rather than numerical artifacts.

Future directions include extension to two- and three-dimensional tumor geometries, incorporation of angiogenesis and drug pharmacokinetics, parameter estimation from clinical imaging data, and application to patient-specific treatment planning for immunotherapy protocols. Computational frameworks of the kind developed here represent a step toward evidence-based tools for predicting individual tumor-immune trajectories and identifying the combination of biological conditions most amenable to immune-mediated tumor control.

As computational models of tumor-immune dynamics grow in clinical relevance, the development of reliable, high-order numerical frameworks of the kind presented here represents a step toward more robust evidence-based tools for cancer treatment policy.

References

1. Adee, S. O.; Onumanyi, P.; Sirisena, U. W.; Yahaya, Y. A. Note on starting the Numerov method more accurately by a hybrid formula of order four for an initial-value problem. *J. Comput. Appl. Math.* **2005**, *175*, 369–373.
2. Akinfenwa, O. A.; Abdulganiy, R. I.; Akinnukawe, B. I.; Okunuga, S. A. Seventh order hybrid block method for solution of first order stiff systems of initial value problems. *J. Egypt. Math. Soc.* **2020**, *28*, 11.
3. Awoyemi, D. O.; Kayode, S. J.; Adoghe, L. O. A five-step P-stable method for the numerical integration of third order ordinary differential equations. *Am. J. Comput. Math.* **2015**, *5*, 136–140.
4. Ayeni, R. O. Mathematical modelling in science and technology. *J. Niger. Math. Soc.* **2004**, *23*, 1–12.
5. Bellomo, N.; Li, N. K.; Maini, P. K. On the foundations of cancer modelling: selected topics, speculations, and perspectives. *Math. Models Methods Appl. Sci.* **2008**, *18*, 593–646.
6. Brugnano, L.; Trigiante, D. *Solving Differential Problems by Multistep Initial and Boundary Value Methods*; Gordon and Breach: Amsterdam, The Netherlands, 1998.
7. Butcher, J. C. A modified multistep method for the numerical integration of ordinary differential equations. *J. ACM* **1965**, *12*, 124–135.
8. Byrne, H. M.; Chaplain, M. A. Modelling the role of cell-cell adhesion in the growth and development of carcinomas. *Math. Comput. Model.* **1996**, *24*, 1–17.
9. Cash, J. R. Efficient numerical methods for the solution of stiff initial-value problems and differential algebraic equations. *Proc. R. Soc. A* **2003**, *459*, 797–815.
10. Chang, C. H.; Qiu, J.; O'Sullivan, D.; Buck, M. D.; Noguchi, T.; Curtis, J. D.; Chen, Q.; Gindin, M.; Gubin, M. M.; van der Windt, G. J. W.; et al. Metabolic competition in the tumor microenvironment is a driver of cancer progression. *Cell* **2015**, *162*, 1229–1241.
11. Chartier, P. L-stable parallel one-block methods for ordinary differential equations. *SIAM J. Numer. Anal.* **1994**, *31*, 552–571.
12. Curtiss, C. F.; Hirschfelder, J. O. Integration of stiff equations. *Proc. Natl. Acad. Sci. USA* **1952**, *38*, 235–243.
13. de Pillis, L. G.; Radunskaya, A. E.; Wiseman, C. L. A validated mathematical model of cell-mediated immune response to tumor growth. *Cancer Res.* **2005**, *65*, 7950–7958.
14. Dunn, G. P.; Bruce, A. T.; Ikeda, H.; Old, L. J.; Schreiber, R. D. Cancer immunoediting: from immunosurveillance to tumor escape. *Nat. Immunol.* **2002**, *3*, 991–998.
15. Eftimie, R.; Bramson, J. L.; Earn, D. J. D. Interactions between the immune system and cancer: a brief review of non-spatial mathematical models. *Bull. Math. Biol.* **2016**, *73*, 2–32.
16. Egwurube, M. O. Stability analysis of nonlinear evolution equations in Banach spaces. *J. Niger. Math. Soc.* **2007**, *26*, 45–62.

17. Engel, K.-J.; Nagel, R. *One-Parameter Semigroups for Linear Evolution Equations*; Springer-Verlag: New York, NY, USA, 2000.
18. Fatunla, S. O. Block methods for second order IVPs. *Int. J. Comput. Math.* **1991**, *41*, 55–63.
19. Ferreira Jr, S. C.; Martins, M. L.; Vilela, M. J. Reaction-diffusion model for the growth of avascular tumor. *Phys. Rev. E* **2002**, *65*, 021907.
20. Gear, C. W. Hybrid methods for initial value problems in ordinary differential equations. *SIAM J. Numer. Anal. Ser. B* **1965**, *2*, 69–86.
21. Gragg, W. B.; Stetter, H. J. Generalized multistep predictor-corrector methods. *J. ACM* **1964**, *11*, 188–209.
22. Hanahan, D.; Weinberg, R. A. Hallmarks of cancer: the next generation. *Cell* **2011**, *144*, 646–674.
23. Hairer, E.; Wanner, G. *Solving Ordinary Differential Equations II: Stiff and Differential-Algebraic Problems*, 2nd ed.; Springer: Berlin, Germany, 1996.
24. Henrici, P. *Discrete Variable Methods in Ordinary Differential Equations*; Wiley: New York, NY, USA, 1962.
25. Kuznetsov, V. A.; Makalkin, I. A.; Taylor, M. A.; Perelson, A. S. Nonlinear dynamics of immunogenic tumors: parameter estimation and global bifurcation analysis. *Bull. Math. Biol.* **1994**, *56*, 295–321.
26. Mambili-Mamboundou, H.; Sibanda, P.; Malinzi, J. Effect of immunotherapy on the response of TICLs to solid tumour invasion. *Math. Biosci.* **2014**, *249*, 52–59.
27. Milne, W. E. *Numerical Solution of Differential Equations*; Wiley: New York, NY, USA, 1953.
28. Motsa, S. Overlapping grid-based optimized single-step hybrid block method for solving first-order initial value problems. *Algorithms* **2022**, *15*, 427.
29. Orakwelu, M. G.; Egwurube, M. O.; Bawa, U. A.; Nwosu, C. On the asymptotic stability and contraction of solutions of an evolution equation. *MATEMATIKA* **2014**, *30*, 185–188.
30. Orakwelu, M. G.; Goqo, S. P.; Motsa, S. S. An optimized two-step block hybrid method with symmetric intra-step points for second order initial value problems. *Eng. Lett.* **2021**, *29*, 948–956.
31. Onumanyi, P.; Sirisena, U. W.; Adee, S. O. Some theoretical considerations of continuous linear multistep methods for $u^{(\ell)} = f(x, u)$, $\ell = 1, 2$. *Bagale J. Pure Appl. Sci.* **2002**, *2*, 1–5.
32. Pazy, A. *Semigroups of Linear Operators and Applications to Partial Differential Equations*; Springer Science & Business Media: New York, NY, USA, 2012.
33. Ramos, H. An optimized two-step hybrid block method for solving first-order initial-value problems in ODEs. *Differ. Geom. Dyn. Syst.* **2017**, *19*, 107–118.
34. Renner, K.; Singer, K.; Koehl, G. E.; Geissler, E. K.; Peter, K.; Siska, P. J.; Kreutz, M. Metabolic hallmarks of tumor and immune cells in the tumor microenvironment. *Front. Immunol.* **2017**, *8*, 248.
35. Rufai, U. O.; Sibanda, P.; Goqo, S. P.; Motsa, S. An overlapping one-step multiderivative hybrid block method for solving second-order initial value problems. *J. Appl. Math.* **2026**, *2026*, 9948007. Available online: <https://doi.org/10.1155/jama/9948007> (accessed on 3 March 2026).
36. Shampine, L. F.; Gladwell, I.; Thompson, S. *Solving ODEs with MATLAB*; Cambridge University Press: Cambridge, UK, 2018.
37. Shampine, L. F.; Watts, H. A. Block implicit one-step methods. *Math. Comput.* **1969**, *23*, 731–740.
38. Sherratt, J. A.; Chaplain, M. A. A new mathematical model for avascular tumour growth. *J. Math. Biol.* **2001**, *43*, 291–312.
39. Stepien, T. L.; Kostelich, E. J.; Kuang, Y. Tumor-immune interaction, surgical treatment, and cancer recurrence in a mathematical model of melanoma. *PLoS Comput. Biol.* **2009**, *5*, e1000362.
40. Voss, D. A.; Abbas, S. Block predictor-corrector schemes for the parallel solution of ODEs. *Comput. Math. Appl.* **1997**, *33*, 65–72.

Disclaimer/Publisher’s Note: The statements, opinions and data contained in all publications are solely those of the individual author(s) and contributor(s) and not of MDPI and/or the editor(s). MDPI and/or the editor(s) disclaim responsibility for any injury to people or property resulting from any ideas, methods, instructions or products referred to in the content.